

A model for water transport in the membrane and an impedance spectroscopy study of the effect of relative humidity on PEM fuel cell parameters

Andrei Kulikovsky^{1, a)} and Tatyana Reshetenko^{2, b)}

¹⁾ Forschungszentrum Jülich GmbH

Theory and Computation of Energy Materials (IET-3)

Institute of Energy and Climate Research,

D-52425 Jülich, Germany

²⁾ Hawaii Natural Energy Institute

University of Hawaii

Honolulu, Hawaii 96822, USA

(Dated: 16 January 2026)

Effective water management is essential for the optimal performance of PEM fuel cells. We have developed an impedance model for liquid water transport through the membrane and coupled it with the two-phase model for cathode side impedance. The complete model was fitted to experimental spectra measured at anode/cathode relative humidities (RH) of 32/32%, 50/50% and 100/100% within a current density range of 100 to 1000 mA cm⁻² and an air flow stoichiometry of 2. Cathode catalyst layer (CCL) saturation decreases with current density due to a growing liquid pressure gradient. For all RH values, the CCL oxygen diffusivity increases dramatically with cell current due to progressive involvement of larger pores into the proton current conversion. Higher RH leads to higher double layer capacitance, which indicates that liquid water increases the electrochemically active surface area.

Keywords: PEM fuel cell, impedance, modeling, relative humidity, oxygen transport

I. INTRODUCTION

Water management is one of the critical issues in optimizing PEM fuel cells performance. Polymer electrolyte in the cathode catalyst layer (CCL) conducts protons only in a wet state. On the other hand, excess of liquid water may severely retard oxygen transport to reaction sites. Water in the CCL arrives from the anode through the membrane and produced in the oxygen reduction reaction (ORR). The balance of water fluxes in the CCL thus depends on the current density, which greatly complicates the problem.

Water management in PEMFCs porous layers has been the subject of numerous experimental and modeling studies (see the review¹). On the modeling side, the problem has been studied using two-phase lattice-Boltzmann modeling (LBM)^{2–6}, pore-network modeling (PNM)^{7–9}, and macro-homogeneous modeling^{10–12}. The most accurate data could potentially be obtained from LBM and PNM, which employ synthetic or reconstructed from experiments porous structures. However, accurately reproducing the CCL structure, which includes carbon particles, platinum species, and ionomer, remains challenging. Furthermore, LBM and PNM are very time-consuming and are therefore not suitable for fitting impedance spectra.

The slowest processes in PEM fuel cells are the dynamics of liquid water in the polymer electrolyte membrane. The water flux through the membrane is the sum of the electroosmotic flux directed from the anode to the cathode,

and the back diffusion flux, which transports water in the opposite direction. The net water flux through the membrane alters the CCL liquid saturation, impacting the CCL impedance.

Electrochemical impedance spectroscopy (EIS) is a powerful tool for analyzing transport processes in PEMFC porous layers¹³. To extract cell transport and kinetic parameters, a relevant physics-based model must be fitted to the experimental spectra. In principle, any transient model of cell performance can be linearized and Fourier-transformed for impedance calculations. However, the key issue for spectra fitting is the speed of model calculations.

One of the first steady-state PEMFC performance models that took into account water transport in the membrane was developed by Springer, Zawodzinski and Gottesfeld¹⁴. The model employed water transport parameters (drag and water diffusion coefficients) that had been measured by the authors. Five years later, Springer et al¹⁵ developed an impedance model of the cell. However, this model ignored water transport in the membrane.

Models of two-phase water transport in the cell vary from one-dimensional through-plane models^{16,17} to multi-dimensional CFD-based models, which take into account the complex geometry of cells^{18–22}. However, very few papers on PEMFC impedance modeling have so far included water dynamics in the membrane. Bao and Bessler calculated the cell impedance using their two-dimensional, two-phase, transient CFD model of PEM fuel cell performance²³. They calculated the response of the cell current to a step-like change of the cell potential and performed a Fourier transform of the applied and response signals to obtain the impedance. To the best of our knowledge, Ref.²³ is the only

^{a)}ECS member; Electronic mail: A.Kulikovsky@fz-juelich.de

^{b)}ECS member; Electronic mail: tatyana@hawaii.edu

work in which the cell impedance was calculated based on a physics-based performance model. However, this time-consuming calculation is not suitable for spectra fitting.

In this work, we have developed a one-dimensional (1d) model for the impedance of the membrane separating the PEMFC anode and cathode. The model is based on a transient equation for water transport through the membrane. The model is coupled with a two-phase impedance model of the cell cathode side^{12,24}. We fitted the complete impedance model to eighteen PEM fuel cell spectra, which were measured at anode/cathode relative humidities of 32/32%, 50/50% and 100/100%, and current densities j_0 of 100, 200, 400, 600, 800 and 1000 mA cm⁻².

Contrary to the common belief, with the growth of j_0 , the CCL mean liquid saturation \bar{s} decreases. This is due to the gradient of the liquid water pressure in the CCL, which increases with the current and effectively removes liquid water from the catalyst layer. The CCL oxygen diffusivity D_{ox} increases dramatically with the cell current. This growth is partly due to the reduction in the CCL liquid saturation. However, the main mechanism behind this increase is the progressive involvement of larger pores in proton current conversion²⁴.

The highest RH of 100/100% provides the highest double layer capacitance and the lowest bulk membrane resistivity. The ORR Tafel slope increases with the cell current, showing significantly larger values observed at 32/32% RH as compared with the other two RH combinations.

II. MODEL FOR MEMBRANE IMPEDANCE

A. Model assumptions and basic equations

The model is based on the following assumptions:

- The cell is isothermal, i.e., the water flux in the membrane due to a temperature gradient is neglected.
- The electroosmotic water drag coefficient n_d in the membrane is constant.
- The gaseous pressure in the CCL is constant. Water evaporation/condensation in the CCL is neglected.
- The membrane water content on the cathode side is the sum of the equilibrium and dynamic terms, as discussed below.
- The static water flux entering the cathode catalyst layer from the membrane is $\alpha_w j_0$, where $\alpha_w = 0.2$ is the net water transfer coefficient and j_0 is the cell current density.

These assumptions are discussed in the text when they are first used.

The liquid water flux N_w in the membrane comprises the diffusion and electroosmotic components:

$$N_w = -D_w \frac{\partial c_w}{\partial x} + \frac{n_d j_0}{F} \quad (1)$$

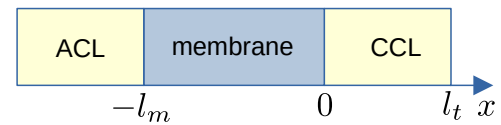


FIG. 1. Schematic of the cell layers and the x -coordinate.

where c_w is the liquid water molar concentration, j_0 is the cell current density, D_w is the membrane liquid water diffusivity, and n_d is the drag coefficient, a number of water molecules transported by one proton.

In the membrane, no charges are produced and hence $\partial j_0 / \partial x = 0$. The continuity equation for c_w is thus

$$\frac{\partial c_w}{\partial t} - \frac{\partial}{\partial x} \left(D_w \frac{\partial c_w}{\partial x} \right) = 0 \quad (2)$$

To simplify the coupling of the membrane model with the CCL performance model, we fix the origin of the x -axis at the membrane / CCL interface. The membrane problem is, therefore, formulated in the domain $x \in [-l_m, 0]$, where l_m is the membrane thickness (Figure 1).

It is convenient to reformulate Eq.(2) in terms of a number of water molecules λ per sulfonic group in the membrane:

$$\lambda = \frac{W_m c_w}{\rho_m} \quad (3)$$

where W_m is the ionomer equivalent weight and ρ_m is the mass density of a dry ionomer. With Eq.(3), equation (2) transforms to

$$\begin{aligned} \frac{\partial \lambda}{\partial t} - \frac{\partial}{\partial x} \left(D_w(\lambda) \frac{\partial \lambda}{\partial x} \right) &= 0, \\ - \frac{\rho_m}{W_m} D_w \frac{\partial \lambda}{\partial x} \Big|_{x=-l_m} + \frac{n_d j_0}{F} &= - \frac{K_L}{V_w \mu_w} \frac{\partial p_L}{\partial x} \Big|_{x=0+}, \\ \lambda|_{x=0-} &= \Lambda(RH^c) + \alpha_s|_{x=0+}. \end{aligned} \quad (4)$$

where the first boundary condition expresses equality of water fluxes on either side of the membrane. Here, K_L is the hydraulic permeability of the CCL, μ_w is the liquid water viscosity, and V_w is the molar volume of water.

The second (right) boundary condition for Eq.(4) is a model assumption meaning that the membrane water content on the cathode side is the sum of two terms. The first term is the static equilibrium water content which depends on the cathode RH via the membrane water sorption isotherm $\Lambda(RH)$ (Figure 3). The second term is proportional to the CCL liquid water saturation. Here, α_s is a dimensionless coefficient on the order of 10, declared below as a fitting parameter. The reason behind this assumption is that the liquid water produced in the ORR wets the CCL membrane phase, which is in contact with the bulk membrane. The ionomer film in the CCL is thin, and its wetting occurs much faster, than the characteristic time for water

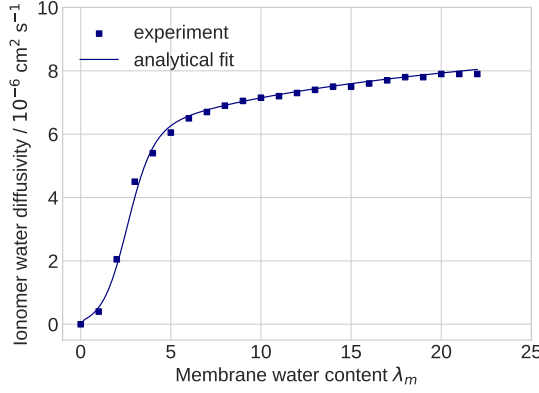


FIG. 2. Points – the diffusion coefficient D_w of water in membrane measured by van Bussel et al.²⁵. Solid line – the analytical fit, Eq.(5).

transport through the bulk membrane. In other words, we assume that any variation in the CCL liquid saturation at the membrane interface affects the water content of the membrane cathode side immediately.

The feature of Eq.(4) is the dependence of the diffusivity D_w on λ_w , which makes Eq.(4) strongly nonlinear. The plot of D_w measured in experiments of van Bussel et al.²⁵ is shown in Figure 2 together with the analytical fit suggested in²⁶:

$$D_w = 4.1 \cdot 10^{-6} \left(\frac{\lambda}{25} \right)^{0.15} \left[1 + \tanh \left(\frac{\lambda - 2.5}{1.4} \right) \right], \text{ cm}^2 \text{s}^{-1} \quad (5)$$

Satterfield and Benziger measured dynamics of the membrane water adsorption by placing a dry membrane in air fully saturated with water vapor²⁷. The characteristic time of membrane wetting was on the order of 1000 s²⁷. This result agrees qualitatively with the D_w curve in Figure 2. Indeed, when the membrane is dry, the characteristic time for water diffusion through the membrane $\tau_D \simeq l_m^2/D_w$ tends to infinity.

The cubic fit for the Nafion membrane water uptake isotherm at 80°C is

$$\Lambda_{RH}(a) = 0.1446 + 11.57a - 17.99a^2 + 16.12a^3 \quad (6)$$

where $a = p_v/p_v^{sat}$ is the water vapor activity (Figure 3). Eq.(6) fits the experimental data of Hinatsu, Mizuhata and Takenaka²⁸. Eq.(6) provides a better fit in the range of $0 \leq a \leq 1$, than the fit²⁶ suggested for the range $0 \leq a \leq 3$.

B. Equation for the perturbation amplitude of the membrane water content

The linearized and Fourier-transformed equation for the dimensionless perturbation amplitude of the membrane wa-

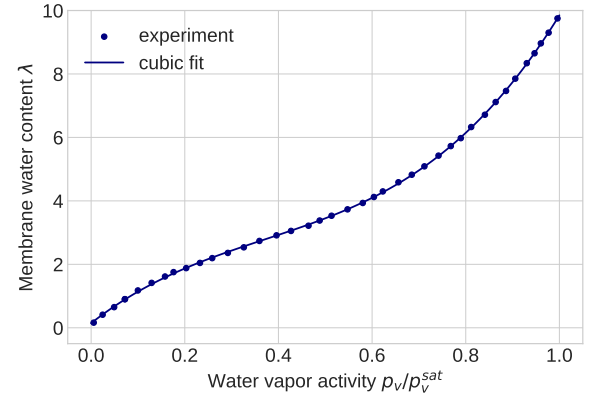


FIG. 3. Points – the membrane water sorption isotherm measured by Hinatsu, Mizuhata and Takenaka²⁸, solid line – Eq.(6). The points were digitized from the best-fit curve provided in Ref.²⁸

ter content is derived in Appendix A:

$$\tilde{D}^0 \frac{\partial^2 \lambda^1}{\partial \tilde{x}^2} + \left(2 \frac{\partial \tilde{D}^0}{\partial \lambda} \frac{\partial \lambda^0}{\partial \tilde{x}} \right) \frac{\partial \lambda^1}{\partial \tilde{x}} + \left(\left(\frac{\partial \lambda^0}{\partial \tilde{x}} \right)^2 \frac{\partial^2 \tilde{D}^0}{\partial \lambda^2} + \frac{\partial \tilde{D}^0}{\partial \lambda} \frac{\partial^2 \lambda^0}{\partial \tilde{x}^2} - i\tilde{\omega} \chi^2 \right) \lambda^1 = 0, \quad (7)$$

Here,

$$\tilde{D} = \frac{4F c_{ref} D}{\sigma_* b}, \quad \tilde{x} = \frac{x}{l_t}, \quad \tilde{\omega} = \omega t_*, \quad \tilde{j} = \frac{j}{j_*}, \quad \tilde{l}_m = \frac{l_m}{l_t} \quad (8)$$

where t_* is the characteristic time of the DL charging, j_* is the characteristic proton current density

$$t_* = \frac{C_{dl} b}{i_*}, \quad j_* = \frac{\sigma_* b}{l_t}, \quad (9)$$

and the dimensionless parameter χ is

$$\chi = \sqrt{\frac{4F c_{ref} i_* l_t^2}{C_{dl} \sigma_* b^2}}. \quad (10)$$

The boundary condition to Eq.(7) on the cathode side of the membrane is

$$\lambda^1|_{\tilde{x}=0-} = \alpha_s s^1|_{\tilde{x}=0+} \quad (11)$$

Eq.(11) means that the perturbation λ^1 changes in-phase with the perturbation of the CCL liquid saturation s^1 , as discussed above. Below, we will see that the solution of Eq.(7) is not needed and the CCL problem is closed using the boundary condition (11).

C. Steady-state problem for water transport in the membrane

The steady-state problem for Eq.(4) in the dimensionless form is

$$\frac{\partial}{\partial \tilde{x}} \left(\tilde{D}^0 \frac{\partial \lambda^0}{\partial \tilde{x}} \right) = 0, \quad \lambda^0|_{\tilde{x}=0-} = \Lambda(RH^c) + \alpha_s s^0|_{\tilde{x}=0+} \\ \left(-A_\lambda \tilde{D}^0 \frac{\partial \lambda^0}{\partial \tilde{x}} \right)|_{\tilde{x}=-\tilde{l}_m} + n_d \tilde{j}^0 = -B_L \frac{\partial \tilde{p}_L^0}{\partial \tilde{x}} \Big|_{\tilde{x}=0+}. \quad (12)$$

Here, the dimensionless parameters A_λ and B_L are

$$A_\lambda = \frac{\rho_m}{4W_m c_{ref}}, \quad B_L = \frac{FK_L p_{O_2}^{ref}}{\mu_w V_w \sigma_* b} \quad (13)$$

and the notations¹² are used.

Experiments of Yan, Toghiani and Wu²⁹ indicate that at RH 100%, the net water flux through the membrane is close to $\alpha_w j_0$, where $\alpha_w \simeq 0.2$. To improve stability of the numerical algorithm, the static water flux was fixed at $\alpha_w j_0$, meaning that the second boundary condition to Eq.(12) was

$$\left(-A_\lambda \tilde{D}^0 \frac{\partial \lambda^0}{\partial \tilde{x}} \right)|_{\tilde{x}=-\tilde{l}_m} + n_d \tilde{j}^0 = \alpha_w \tilde{j}_0 \quad (14)$$

Integrating Eq.(12) from $-\tilde{l}_m$ to \tilde{x} , we get the first-order equation expressing conservation of the diffusive water flux in the membrane

$$\tilde{D}^0 \frac{\partial \lambda^0}{\partial \tilde{x}} = p, \quad \lambda^0|_{\tilde{x}=0-} = \Lambda(RH^c) + \alpha_s s^0|_{\tilde{x}=0+} \quad (15)$$

where

$$p = \tilde{D}^0 \frac{\partial \lambda^0}{\partial \tilde{x}} \Big|_{\tilde{x}=-\tilde{l}_m}. \quad (16)$$

The parameter p can be determined from Eq.(14):

$$p = \frac{(n_d - \alpha_w) \tilde{j}_0}{A_\lambda} \quad (17)$$

With Eq.(17), equation (15) forms a Cauchy problem. If necessary, it can be solved backward, from $\tilde{x} = 0$ to $\tilde{x} = -\tilde{l}_m$, using a standard Runge-Kutta method. However, the impedance problem requires only the membrane water content and its first derivative at $\tilde{x} = 0$ (see below). These values can be calculated directly from the equations of this section:

$$\lambda^0|_{\tilde{x}=0-} = \Lambda(RH^c) + \alpha_s s^0|_{\tilde{x}=0+}, \\ \frac{\partial \lambda^0}{\partial \tilde{x}} \Big|_{\tilde{x}=0-} = \frac{p}{\tilde{D}^0(\lambda^0|_{\tilde{x}=0-})} \quad (18)$$

Transport equations	
$\frac{\partial c_h}{\partial t} + v \frac{\partial c_h}{\partial z} = -\frac{D_b}{h} \frac{\partial c_b}{\partial x} \Big _{x=l_t+l_b} \quad (19)$	Channel
$\frac{\partial c_b}{\partial t} - D_b \frac{\partial^2 c_b}{\partial x^2} = 0 \quad (20)$	GDL
$\frac{\partial c}{\partial t} - \frac{\partial}{\partial x} \left(D_{ox} \frac{\partial c}{\partial x} \right) = -\frac{Q_{ORR}}{4F} \quad (21)$ $C_{dl} \frac{\partial \eta}{\partial t} - \frac{\partial}{\partial x} \left(\sigma_p \frac{\partial \eta}{\partial x} \right) = -Q_{ORR} \quad (22)$ $\frac{1}{V_l} \frac{\partial s}{\partial t} - \frac{K_l}{V_l \mu_l} \frac{\partial^2 p_l}{\partial x^2} = \frac{Q_{ORR}}{2F} \quad (23)$	CCL
Source function	
$Q_{ORR} = i_* \left(\frac{c}{c_{ref}} \right) \exp \left(\frac{\eta}{b} \right) \quad (24)$	ORR rate
Water retention curve (WRC) and the CCL transport coefficients	
$s = s_0 + \frac{(1-s_0)}{2} \left(1 + \tanh \left(\frac{p_c - p_{c,0}}{k_{pc}} \right) \right) \quad (25)$	WRC
$\sigma_p = k_\sigma s \quad (26)$	H^+ conductivity
$D_{ox} = D_{ox,d} (1-s)^3 \quad (27)$	O_2 diffusivity

TABLE I. Eqs.(19)–(21), the governing equations for oxygen, water and proton transport. GDL stands for the gas diffusion layer. Eq.(24) is the ORR rate. Eqs.(25),(26), (27) – the WRC, proton conductivity vs saturation, and the oxygen diffusivity vs saturation, respectively. For the notations see Nomenclature section.

III. MODEL FOR THE CATHODE SIDE IMPEDANCE

The core of the cathode side impedance model with the two-phase water transport in the CCL was developed by Sun et al.¹². The model equations are listed in Table I; for the notations see the Nomenclature section. The cell performance model¹² includes through-plane equations for

the oxygen, proton and water transport, Eqs.(20)–(23).

A model extension that takes into account the convective air transport in the channel, Eq.(19), is reported in Reshetenko et al.²⁴. This extension is particularly important at the low air flow stoichiometry of $\lambda_c = 2$ used in this work, as the local current and oxygen distributions along the channel are strongly nonuniform. The local current density distribution along the channel was calculated using the model³⁰. It is worth noting that in^{24,30} the quadratic dependence of the CCL effective oxygen diffusivity D_{ox} on the parameter $(1 - s)$ in Eq.(27) was used. Here, however, we used the cubic dependence, as with the scaling $(1 - s)^2$ we were unable to achieve a satisfactory fit to the low-frequency part of the spectra below 1 Hz.

The boundary conditions express the continuity of oxygen concentration and flux at the channel/gas diffusion layer (GDL) and GDL/CCL interfaces, as well as the influx of liquid water from the membrane to the CCL (see below). They also represent zero oxygen flux in the membrane and zero proton current at the CCL/GDL interface. Further details can be found in^{12,24}. The 1d+1d performance model in Table I was linearized and Fourier-transformed to obtain the linear boundary-value problem for the small perturbation amplitudes of the oxygen concentration and ORR overpotential. In this work, we set the water vapor concentration in the CCL equal to the saturated value, $c_v = c_v^{sat}$. This is equivalent to zero evaporation/condensation rates.

The $5 \times 5 \text{ cm}^2$ meander flow field was modeled as a single straight channel divided into eight segments. The through-plane equations were linked to the oxygen transport equation in the channel using a 1d+1d approach. In each segment, solving the through-plane problem yields the local segment impedance Z_{seg} :

$$Z_{seg} = - \frac{\eta^1}{\sigma_p \partial \eta^1 / \partial x} \Big|_{x=0} \quad (28)$$

where $x = 0$ corresponds to the membrane interface, η^1 is the overpotential perturbation and σ_p is the CCL proton conductivity. The segments are connected in parallel and the total cell impedance was calculated as

$$Z_{cell} = \left(\frac{1}{8} \sum_{n=1}^8 \frac{1}{Z_{seg,n}} \right)^{-1} + i\omega L_{cab} S_{cell} + R_{HFR} \quad (29)$$

where L_{cab} is the cable inductance, S_{cell} is the cell active area, and R_{HFR} is the high-frequency (ohmic) cell resistance.

IV. MODELS COUPLING AND NUMERICAL ASPECTS

The membrane water content λ and water flux must be coupled with the saturation and water flux in the CCL. Consider first the steady-state solutions in the membrane and CCL. The dimensionless static equation for the liquid pres-

sure \tilde{p}_L^0 in the CCL, Eq.(23), reads

$$-\tilde{k}_L \frac{\partial^2 \tilde{p}_L^0}{\partial \tilde{x}^2} = 2\tilde{p}_{O_2}^0 e^{\tilde{\eta}^0},$$

$$-B_L \frac{\partial \tilde{p}_L^0}{\partial \tilde{x}} \Big|_{\tilde{x}=0+} = \alpha_w \tilde{j}_0, \quad \tilde{p}_L^0|_{\tilde{x}=1} = \tilde{p}_{cell} \quad (30)$$

where the boundary condition at $\tilde{x} = 0$ fixes the static water flux entering from the membrane to the CCL. Here,

$$\tilde{k}_L = \frac{4F p_{O_2} K_L}{i_* l_t^2 \mu_w V_w} \quad (31)$$

and the other parameters appearing in Eq.(13) are described in the Nomenclature section.

The problem for the small perturbation amplitude \tilde{p}_L^1 at the membrane/CCL interface¹² reads

$$\tilde{k}_L \frac{\partial^2 \tilde{p}_L^1}{\partial \tilde{x}^2} = \gamma^2 i \tilde{\omega} s^1 - 2e^{\tilde{\eta}^0} (\tilde{p}_{O_2}^1 + \tilde{p}_{O_2}^0 \tilde{\eta}^1),$$

$$-B_L \frac{\partial \tilde{p}_L^1}{\partial \tilde{x}} \Big|_{\tilde{x}=0+}$$

$$= \left(-A_\lambda \left(\tilde{D}^0 \frac{\partial \lambda^1}{\partial \tilde{x}} + \frac{\partial D^0}{\partial \lambda} \frac{\partial \lambda^0}{\partial \tilde{x}} \lambda^1 \right) + n_d \tilde{j}^1 \right)_{\tilde{x}=0-},$$

$$\tilde{p}_L^1|_{\tilde{x}=1} = 0 \quad (32)$$

where the first boundary condition means continuity of the water flux perturbations on either side of the membrane/CCL interface. Here, γ is the constant parameter

$$\gamma = \sqrt{\frac{4F}{V_w C_{dl} b}}, \quad (33)$$

Using Eq.(11) in the first boundary condition to Eq.(32), this condition is reformulated in terms of the perturbation amplitude of CCL liquid saturation s^1 :

$$-B_L \frac{\partial \tilde{p}_L^1}{\partial \tilde{x}} \Big|_{\tilde{x}=0+}$$

$$= \left(-A_\lambda \alpha_s \left(\tilde{D}^0 \frac{\partial s^1}{\partial \tilde{x}} + \frac{\partial D^0}{\partial \lambda} \frac{\partial \lambda^0}{\partial \tilde{x}} s^1 \right) + n_d \tilde{j}^1 \right)_{\tilde{x}=0-},$$

$$(34)$$

Eq.(34) closes the problem for the small perturbation amplitudes in the CCL. The relaxation of the membrane water content appears in the model through the coefficients in Eq.(34), which are derived from Eq.(18). Eq.(34) is the only correction to the model for the perturbation amplitudes discussed in Sun et al.¹². A complete formulation of the latter problem can be found in Appendix D of Ref.¹².

The custom fitting code was developed using the Python SciPy library and the MPI library for parallel calculations. Solution of the static problems for the membrane, Eq.(15), and CCL, Eqs.(30), does not require iterations. The static membrane problem was solved using the Runge-Kutta solver `solve_ivp`. The linear boundary-value problems (BVPs) for

Cathode pressure, bar	1.5
Anode/cathode RH, %	32/32, 50/50, 100/100
Cell temperature, K	273 + 80
Hydrogen/air flow stoichiometry	2/2 (2/4 for 100 mA cm ⁻²)
CCL thickness μm	10
GDL thickness μm	235

TABLE II. The regime of cell operation and the estimated thicknesses of the CCL and GDL.

the perturbation amplitudes and the nonlinear BVPs for the static variables (pressures and overpotential) were solved using the *solve_bvp* SciPy solver.

Eq.(29) was fitted to the experimental spectra using the SciPy least-squares module *least_squares*. Fitting of a single spectrum with 96 frequency points takes around five minutes on 48 cores of a parallel cluster with Intel Xeon processors, or around half an hour on an eight-core notebook.

V. EXPERIMENTAL

The experimental work was performed at Hawaii Natural Energy Institute (HNEI) using a custom-built fuel cell test station and a proprietary impedance spectroscopy system. Catalyst coated membranes with a geometric area of 25 cm² were supplied by Gore. The Pt loading was 0.4 mg_{Pt} cm⁻² for both the anode and cathode. The membrane electrode assembly (MEA) utilized 25 BC GDLs for both electrodes and Teflon gaskets with a thickness of 150 μm , providing a 20% compression ratio.

A 25 cm² single cell hardware was manufactured at Fuel Cell Technology Inc. The flow field design featured a triple serpentine configuration for both the anode and cathode, with channels 0.787 mm wide and 1.02 mm deep, and ribs 0.787 mm wide. A co-flow gas arrangement was employed throughout this study.

The anode and cathode feed gases were humidified to the desired level, and the cell was operated at a backpressure of 1.5 bar and a temperature of 80°C. Minimum gas flow rates were fixed to provide a stoichiometry of 2 at 200 mA cm⁻². Thus, the reactant stoichiometry was 2 for H₂ and air at current densities above 200 mA cm⁻², while at 100 mA cm⁻² the stoichiometry was increased to 4. The operating conditions are summarized at Table II.

EIS was conducted under galvanostatic load control in a frequency range of 10 kHz to 0.1 Hz using 20 points per decade. The amplitude of current perturbation was selected such that the amplitude of cell voltage oscillations remained below 10 mV.

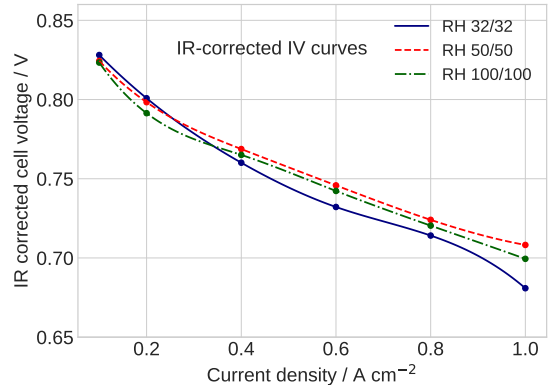


FIG. 4. The experimental (points) and interpolated (lines) IR-corrected polarization curves of the cell operated at the indicated relative humidities. The points are interpolated using cubic spline just as an eye guide.

VI. RESULTS AND DISCUSSION

Figure 4 shows the IR-corrected polarization curves of the cell operating with the anode/cathode relative humidity of 32/32%, 50/50% and 100/100%. These curves were measured at the current densities corresponding to those at which the impedance spectra were acquired. As can be seen, the difference between the IR-corrected cell potentials does not exceed 15 mV (Figure 4). One might expect the impedance spectra measured at the same currents and different RH values to produce similar cell parameter values, except for high-frequency cell resistivity.

Figure 5 shows the experimental and fitted model Nyquist spectra for RH 100/100%. The model fits the spectra well. The spectra for RH 32/32% and 50/50% are fitted equally well. A more detailed plot of the experimental and fitted model spectra is shown in Figure 6.

Figure 7 shows the dependence of the fitted cell parameters on the current density. The error bars in Figure 7 were calculated from the Jacobian matrix returned by the *least_squares* procedure. The size of the error bar indicates how sensitive the fitted spectrum is to variation in the respective parameter. A small bar indicates high sensitivity and vice versa.

In general, the curves for different RH demonstrate similar trends, with important variations discussed below. This similarity gives us confidence that the model correctly captures key phenomena in the cell.

Contrary to common belief, the CCL mean liquid saturation decreases with the cell current density for all three RH values (Figure 7a). This decrease is due to the liquid pressure gradient in the CCL, which increases linearly with the cell current and removes liquid water from the catalyst layer (Figure 7b).

The through-plane shapes of the liquid saturation and the liquid pressure gradient for RH 32/32% and RH 100/100% are shown in Figures 8 and 9, respectively. The effect of

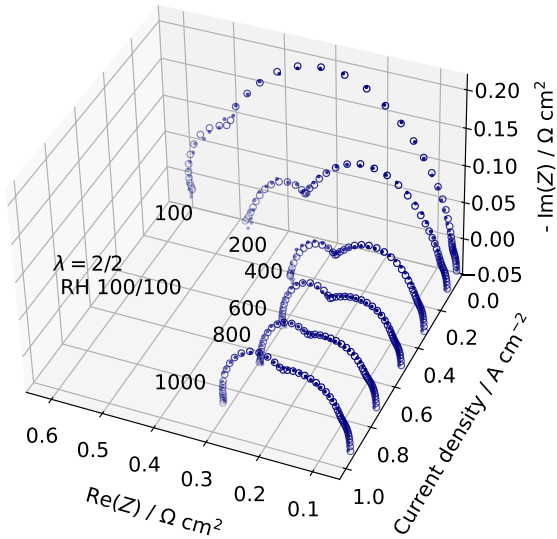


FIG. 5. The experimental spectra (points) and fitted model Eq.(29) (open circles) for the indicated current densities (mA cm^{-2}). To improve readability, half of the points (10 per decade) are shown. The regime of cell operation is indicated in Table II, RH 32/32%.

reducing s at currents 0.8 A cm^{-2} (solid red curve) and 1.0 A cm^{-2} (dashed blue curve) is clearly visible. Furthermore, at RH 32/32% and high currents, the saturation is much less uniform along the \tilde{x} -coordinate (Figure 8a).

At all RH values, the CCL effective oxygen diffusivity D_{ox} exhibits rapid growth with the cell current density (Figure 7c). This growth is partly due to the decreasing liquid saturation, see Eq.(27). However, the most significant factor contributing to this growth is the progressive involvement of larger pores in the process of current conversion. As discussed by Reshetenko et al.²⁴, a small current is converted in the smallest pores due to their large surface area. The Knudsen oxygen diffusivity of small pores is proportional to their radius. As the current grows, larger pores become involved in the current conversion process, leading to an increase in the effective diffusivity as measured by EIS.

The in-situ parameter D_{ox} measured here should not be confused with the ex-situ CCL diffusivity measured, for example, by Suzuki et al.³¹ using a microfluidic device. In the ex-situ experiment³¹, the measured diffusivity of gaseous oxygen through the void CCL pores is more than two orders of magnitude higher than the CCL oxygen diffusivity shown in Figure 7c. In an operating PEM fuel cell, the oxygen transport pathway to Pt surface includes the ionomer film barrier covering the Pt/C agglomerates and the diffusion inside the agglomerates, which are filled with water. These transport elements dramatically reduce the effective oxygen diffusivity in the operating CCL as compared to the ex-situ values.

The GDL oxygen diffusivity D_b varies between 0.02 and $0.04 \text{ cm}^2 \text{ s}^{-1}$ depending on the RH value (Figure 7d). At currents of 100 and 200 mA cm^{-2} , the contribution of oxy-

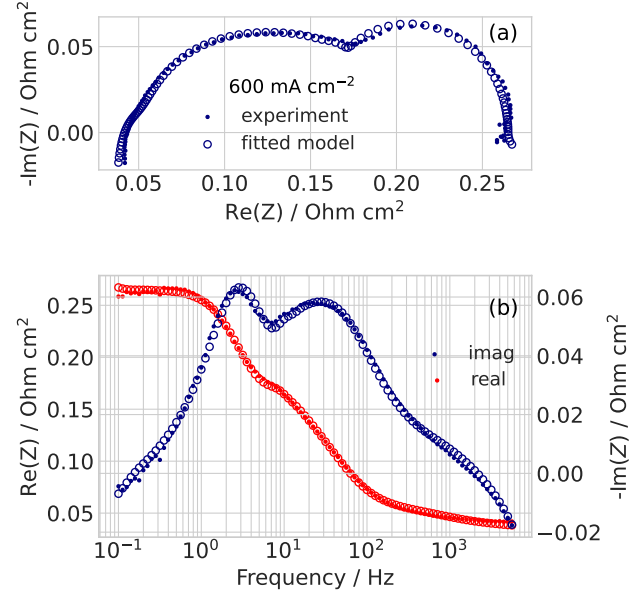


FIG. 6. The experimental spectra (points) and fitted model Eq.(29) (open circles) for the current density of 600 mA cm^{-2} and RH 100/100%.

gen transport in the GDL to the cell impedance is negligible and cannot be captured by the model.

The ORR Tafel slope increases with the cell current density from 60 to 150 mV/decade (Figure 7e). At the lowest RH 32/32%, the Tafel slope is notably higher than at the other two RH combinations, suggesting that liquid water accelerates some of the reaction steps in the ORR.

The CCL proton conductivity σ_p varies from 10 to 20 mS cm^{-1} , with notably lower values at RH 32/32% (Figure 7f). At RH 50/50% and 100/100%, σ_p decreases with the cell current, following the CCL liquid saturation. Note the significant decay of σ_p at RH 32/32% and a cell current density of 1000 mA cm^{-2} (Figure 7f, the blue curve). This decay, together with the increasing ORR Tafel slope (Figure 7d) is responsible for the bending of the blue polarization curve in Figure 4.

The parameters sensitive to relative humidity are the DL capacitance, which increases with RH (Figure 7g) and the high-frequency (ohmic) cell resistivity, which decreases with RH (Figure 7h). The positive effect of water on DL capacitance suggests that water increases the electrochemically active surface area (ECSA). This behavior correlates with the results of CO stripping experiments of Shinozaki, Yamada and Morimoto³², which indicate a steady increase in Pt utilization as RH changes from 25% to 100%.

The high-frequency (ohmic) cell resistance depends weakly on the cell current and strongly on the RH (Figure 7h). The key factor here is the *anodic* RH. The large HFR resistance at RH 32/32% (Figure 7h) shows that the

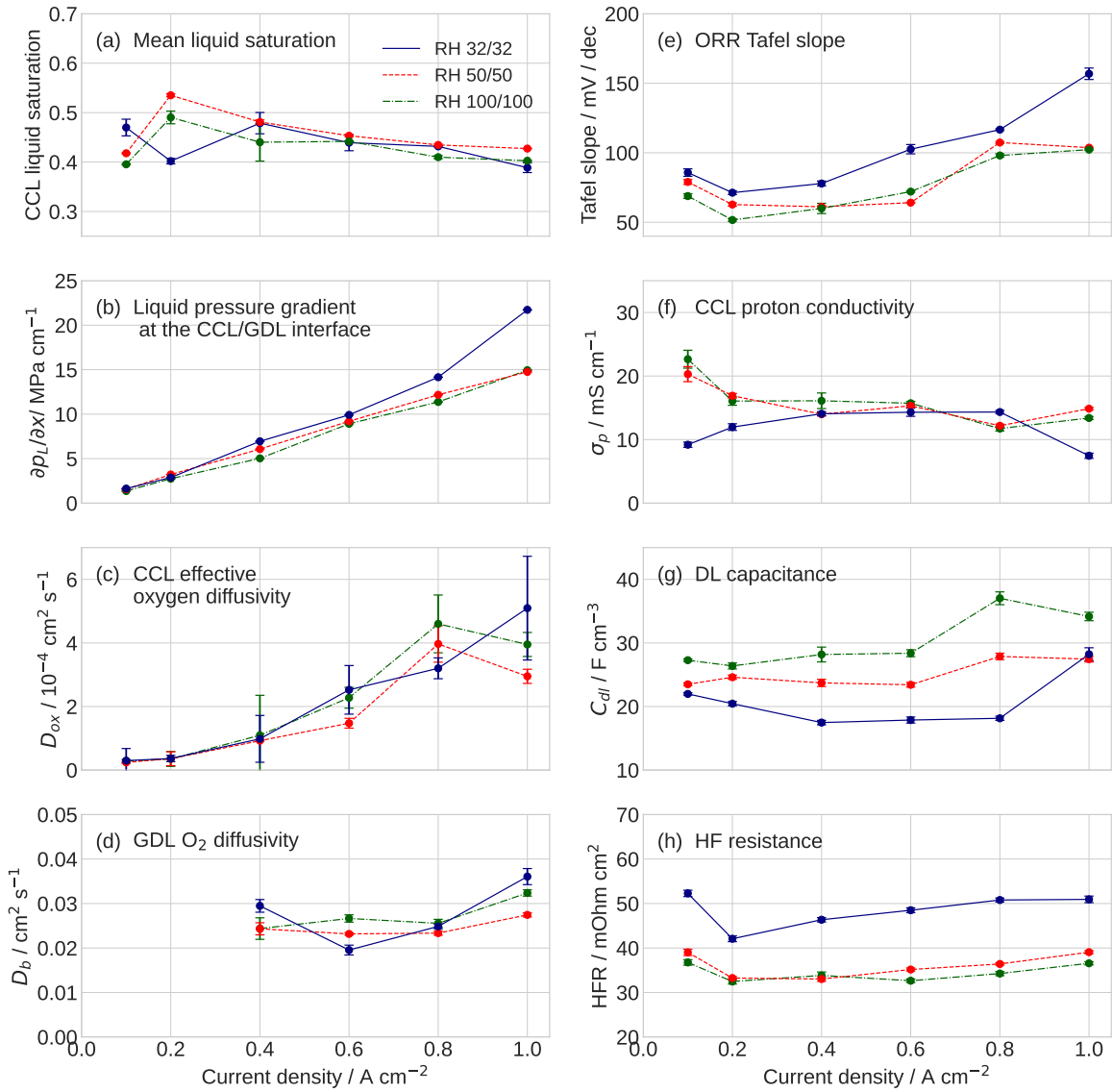


FIG. 7. The dependence of fitted parameters on the cell current density at RH 32/32%, 50/50%, and 100/100%. The lines are only intended as a guide.

liquid water back diffusion from the CCL to the anode side is small, meaning that the membrane can only be humidified from the anode side. Indeed, the effective diffusivity of liquid water in the Nafion membrane decreases as the membrane water content falls (Figure 2). Thus, the electroosmotic drag of water drying out the anode side of the membrane simultaneously lowers the water diffusivity there. Once the anode side of the membrane is dry, it cannot be humidified by water back diffusion from the cathode side²⁶. This effect is the main reason why, in practical applications, the anode flow RH is typically kept above 50%.

Finally, the data in Figures 7c,d allow us to compare the characteristic frequencies of the oxygen transport in the GDL f_{GDL} and the CCL f_{CCL} . For the estimation we use the Warburg finite-length formula for the characteristic

frequency f of mass transport in the porous layer

$$f = \frac{0.404D}{l^2}, \quad (35)$$

where D is the oxygen diffusivity of the porous layer and l is the layer thickness. The result is shown in Figure 10. As can be seen, f_{CCL} is close to f_{GDL} at the current density of 100 mA cm⁻². At this current density, the DRT would produce a single oxygen transport peak representing the O₂ transport in both the layers. However, as the current density increases, f_{CCL} increases linearly, while f_{GDL} remains almost constant at around 10 Hz. At a cell current of 1 A cm⁻², f_{CCL} is an order of magnitude larger than f_{GDL} (Figure 10). Thus, as the cell current increases, the frequency f_{CCL} overlaps with the ORR charge-transfer fre-

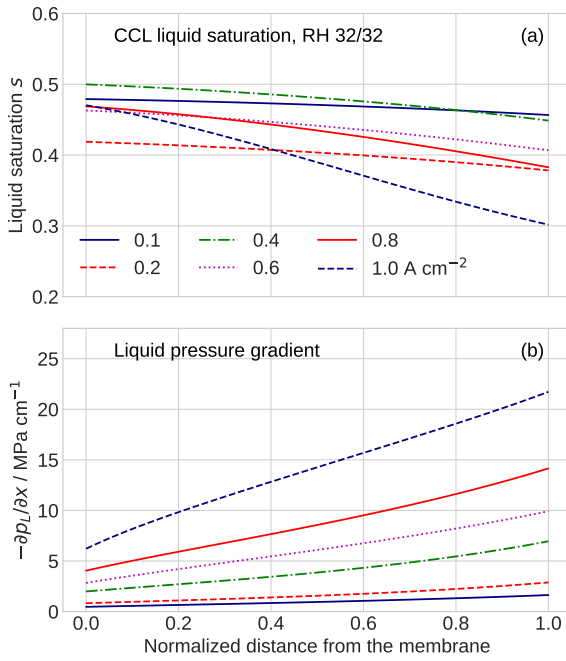


FIG. 8. The shapes of (a) the liquid saturation and (b) the (negative) liquid pressure gradient through the CCL depth for RH 32/32% and the indicated current densities (A cm^{-2}).

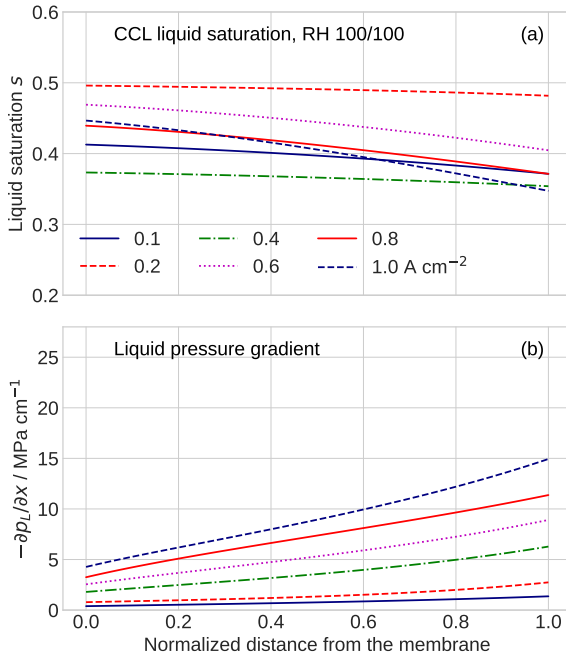


FIG. 9. The shapes of (a) the liquid saturation and (b) the (negative) liquid pressure gradient through the CCL depth for RH 100/100% and the indicated current densities (A cm^{-2}).

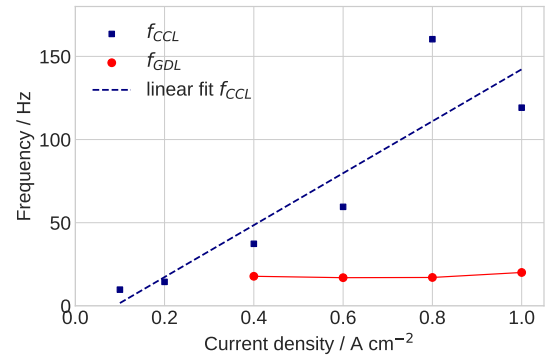


FIG. 10. The characteristic frequencies of the oxygen transport in the CCL (blue squares and the dotted line) and in the GDL (red filled circles and the solid line) vs the cell current density for RH 100/100%.

frequency, and may even exceed it. This effect should be taken into account in the DRT analyses of PEMFC spectra.

VII. CONCLUSIONS

We developed a model of the membrane impedance in a PEM fuel cell. This model was then coupled with a recent two-phase model for the cell cathode impedance. We fitted the complete model to measured spectra of a PEMFC operated at three relative humidities of 32/32%, 50/50% and 100/100%. Six spectra were acquired for each RH combination at current densities ranging from 100 to 1000 mA cm^{-2} . The dependence of the fitting parameters on the cell current shows the following trends.

- The mean CCL liquid saturation \bar{S} decreases with the cell current in the range of 600 to 1000 mA cm^{-2} .
- The decrease in liquid saturation is due to the growing liquid pressure gradient, which removes water from the CCL.
- The CCL effective oxygen diffusivity D_{ox} increases dramatically with the cell current. Following Ref²⁴, we attribute this growth to the progressive involvement of larger pores to the proton current conversion.
- The ORR Tafel slope increases with the cell current from 60 to 150 mV/decade. At RH 32/32%, the Tafel slope is significantly higher than at the other two RH combinations.
- The CCL proton conductivity σ_p is about 15 mS cm^{-1} . At RH 50/50% and 100/100%, it decreases with the cell current. At RH 32/32%, σ_p shows no clear correlation with the current density.
- The double layer capacitance increases with the RH indicating growth of the ECSA with the RH. This effect correlates with the experiments³².

- The GDL oxygen diffusivity, which is in the range of 0.02 to 0.04 $\text{cm}^2 \text{ s}^{-1}$ is almost independent of the current density.
- At RH 32/32%, the high-frequency cell resistivity is significantly higher, than at RH 50/50% and 100/100%. This indicates poor wetting of the anode side of the membrane by water back diffusion from the cathode side. We attribute this effect to the reduction in ionomer water diffusivity as the water content decreases.

VIII. ACKNOWLEDGMENTS

T. Reshetenko gratefully acknowledges funding from the US Office of Naval Research (N00014-25-1-2372).

Appendix A: Equation for the perturbation amplitude of the membrane water content

To linearize Eq.(4) we substitute into Eq.(4) $D_w = D_w^0(x) + D_w^1(x, t)$, $\lambda = \lambda^0(x) + \lambda^1(x, t)$, neglect products of the small terms and subtract the static equation for λ^0 . For the small-amplitude transient $\lambda^1(x, t)$ we find the equation

$$\frac{\partial \lambda^1}{\partial t} - \left(2 \frac{\partial D^0}{\partial \lambda} \frac{\partial \lambda^0}{\partial x} \right) \frac{\partial \lambda^1}{\partial x} - \left(\frac{\partial \lambda^0}{\partial x} \right)^2 \frac{\partial D^1}{\partial \lambda} - D^1 \frac{\partial^2 \lambda^0}{\partial x^2} - D^0 \frac{\partial^2 \lambda^1}{\partial x^2} = 0 \quad (\text{A1})$$

Using $D^1 = (\partial D^0 / \partial \lambda) \lambda^1$, $\partial D^1 / \partial \lambda = (\partial^2 D^0 / \partial \lambda^2) \lambda^1$, and substituting into Eq.(A1) the Fourier-transform

$$\lambda^1(x, t) = \lambda^1(x, \omega) \exp(i\omega t), \quad (\text{A2})$$

we get the equation for the perturbation amplitude $\lambda^1(x, \omega)$:

$$D^0 \frac{\partial^2 \lambda^1}{\partial x^2} + \left(2 \frac{\partial D^0}{\partial \lambda} \frac{\partial \lambda^0}{\partial x} \right) \frac{\partial \lambda^1}{\partial x} + \left(\left(\frac{\partial \lambda^0}{\partial x} \right)^2 \frac{\partial^2 D^0}{\partial \lambda^2} + \frac{\partial D^0}{\partial \lambda} \frac{\partial^2 \lambda^0}{\partial x^2} - i\omega \right) \lambda^1 = 0 \quad (\text{A3})$$

It is convenient to transform Eq.(A3) using the dimensionless variables¹². Multiplying Eq.(A3) by $4F c_{ref} l_t^2 / (\sigma_* b)$, we get Eq.(7).

¹²Ö. F. Günaydin, S. Topçu, and A. Aksoy. A review of proton exchange membrane fuel cell water management: Membrane electrode assembly. *J. Power Sources*, 517:230723, 2022. doi: 10.1016/j.jpowsour.2021.230723.

²P. P. Mukherjee, C.-Y. Wang, and Q. Kang. Mesoscopic modeling of two-phase behavior and flooding phenomena in polymer electrolyte fuel cells. *Electrochimica Acta*, 54:6861–6875, 2009. doi: 10.1016/j.electacta.2009.06.066.

³G. R. Molaeimanesh, M. A. Bamdezh, and M. Nazemian. Impact of catalyst layer morphology on the performance of PEM fuel cell cathode via lattice Boltzmann simulation. *Int. J. Hydrogen Energy*, 43:20959–20975, 2018. doi:10.1016/j.ijhydene.2018.09.076.

⁴P. Satjaritanun, S. Hirano, I. V. Zenyuk, and S. Shimpalee. Numerical study of electrochemical kinetics and mass transport inside nano-structural catalyst layer of pemfc using lattice Boltzmann agglomeration method. *J. Electrochem. Soc.*, 167:013516, 2020. doi: 10.1149/2.0162001JES.

⁵J. B. Grunewald, N. Goswami, P. P. Mukherjee, and T. F. Fuller. Two-phase dynamics and hysteresis in the PEM fuel cell catalyst layer with the lattice-Boltzmann method. *J. Electrochem. Soc.*, 168: 024521, 2021. doi:10.1149/1945-7111/abe5e8.

⁶L. Chen, Q. Kang, and W. Tao. Pore-scale numerical study of multiphase reactive transport processes in cathode catalyst layers of proton exchange membrane fuel cells. *Int. J. Hydrogen Energy*, 46: 13283–13279, 2021. doi:10.1016/j.ijhydene.2021.01.146.

⁷M. El Hannach, M. Prat, and J. Pauchet. Pore network model of the cathode catalyst layer of proton exchange membrane fuel cells: Analysis of water management and electrical performance. *Int. J. Hydrogen Energy*, 37:18996–19006, 2012. doi: 10.1016/j.ijhydene.2012.09.139.

⁸R. Wu, Q. Liao, X. Zhu, and H. Wang. Pore network modeling of cathode catalyst layer of proton exchange membrane fuel cell. *Int. J. Hydrogen Energy*, 37:11255–11267, 2012. doi: 10.1016/j.ijhydene.2012.04.036.

⁹R. van Gorp, M. van der Heijden, M. A. Sadeghi, J. Gostick, and A. Forner-Cuenca. Bottom-up design of porous electrodes by combining a genetic algorithm and a pore network model. *Chem. Eng. J.*, 455:139947, 2023. doi:10.1016/j.cej.2022.139947.

¹⁰M. Eikerling. Water management in cathode catalyst layers of PEM fuel cells. *J. Electrochem. Soc.*, 153:E58–E70, 2006. doi: 10.1149/1.2160435.

¹¹W. Olbrich, T. Kadyk, U. Sauter, and M. Eikerling. Modeling of wetting phenomena in cathode catalyst layers for PEM fuel cells. *Electrochimica Acta*, 431:140850, 2022. doi: 10.1016/j.electacta.2022.140850.

¹²Y. Sun, T. Kadyk, A. Kulikovsky, and M. Eikerling. The effect of liquid saturation transients on PEM fuel cell impedance: Inductive loop and instability of catalyst layer operation. *J. Electrochem. Soc.*, 171:074506, 2024. doi:10.1149/1945-7111/ad5efd.

¹³A. Lasia. *Electrochemical Impedance Spectroscopy and its Applications*. Springer, New York, 2014.

¹⁴T. E. Springer, T. A. Zawodzinski, and S. Gottesfeld. Polymer electrolyte fuel cell model. *J. Electrochem. Soc.*, 138(8):2334–42, 1991.

¹⁵T. E. Springer, T. A. Zawodzinski, M. S. Wilson, and S. Gottesfeld. Characterization of polymer electrolyte fuel cells using AC impedance spectroscopy. *J. Electrochem. Soc.*, 143:587–599, 1996. doi:10.1149/1.1836485.

¹⁶F. Chen, M.-H. Chang, and C.-F. Fang. Analysis of water transport in a five-layer model of PEMFC. *J. Power Sources*, 164:649–658, 2007. doi:10.1016/j.jpowsour.2006.10.072.

¹⁷P. O. Olapade, J. P. Meyers, R. Mukundan, J. R. Davey, and R. L. Borup. Modeling the dynamic behavior of proton-exchange membrane fuel cells. *J. Electrochem. Soc.*, 158:B536–B549, 2011. doi: 10.1149/1.3559491.

¹⁸D. Natarajan and T. V. Nguyen. A two-dimensional, two-phase, multicomponent, transient model for the cathode of a proton exchange membrane fuel cell using conventional gas distributors. *J. Electrochem. Soc.*, 148(12):A1324–A1335, 2001. doi: 10.1149/1.1415032.

¹⁹Y. Wang and C.-Y. Wang. Two-phase transients of polymer electrolyte fuel cells. *J. Electrochem. Soc.*, 154(7):B636–B643, 2007. doi:10.1149/1.2734076.

²⁰V. Gurau, Th. A. Zavodzinski Jr., and J. A. Mann Jr. Two-phase transport in PEM fuel cell cathodes. *J. Fuel Cell Sci. Techn.*, 5: 021009–1–021009–12, 2008. doi:10.1115/1.2821597.

²¹H. Wu, P. Berg, and X. Li. Modeling of PEMFC transients with finite-rate phase-transfer processes. *J. Electrochem. Soc.*, 112:B1–B12, 2010. doi:10.1149/1.3248005.

²²T. Berning, M. Odgaard, and S. K. Kaer. Water balance simulations of a polymer-electrolyte membrane fuel cell using a two-fluid model. *J. Power Sources*, 196:6305–6317, 2011. doi: 10.1016/j.jpowsour.2011.03.068.

²³C. Bao and W. G. Bessler. Two-dimensional modeling of a polymer electrolyte membrane fuel cell with long flow channel. Part II. physics-based electrochemical impedance analysis. *J. Power Sources*, 278:675–682, 2015. doi:10.1016/j.jpowsour.2014.12.045.

²⁴T. Reshetenko, Y. Sun, T. Kadyk, M. Eikerling, and A. Kulikovsky. An impedance spectroscopy study to unravel the effect of water on proton and oxygen transport in PEM fuel cells. *Electrochim. Acta*, 507:145172, 2024. doi:10.1016/j.electacta.2024.145172.

²⁵H. P. L. H. van Bussel, F. G. H. Koene, and R. K. A. M. Mallant. Dynamic model of solid polymer fuel cell water management. *J. Power Sources*, 71:218–22, 1998. doi:/10.1016/S0378-7753(97)02744-4.

²⁶A. A. Kulikovsky. Quasi-3d modeling of water management in polymer electrolyte fuel cell. *J. Electrochem. Soc.*, 150(11):A1432–A1439, 2003. doi:10.1149/1.1611489.

²⁷M. B. Satterfield and J. B. Benziger. Non-fickian water vapor sorption dynamics by nafton membranes. *J. Phys. Chem. B*, 112:3693–3704, 2008. doi:10.1021/jp7103243.

²⁸J. T. Hinatsu, M. Mizuhata, and H. Takenaka. Water uptake of perfluorosulfonic acid membranes from liquid water and water vapor. *J. Electrochem. Soc.*, 141(6):1493–8, 1994. doi:10.1149/1.2054951.

²⁹Q. Yan, H. Toghiani, and J. Wu. Investigation of water transport through membrane in a PEM fuel cell by water balance experiments. *J. Power Sources*, 158:316–325, 2006. doi: 10.1016/j.jpowsour.2005.09.013.

³⁰T. Reshetenko and A. Kulikovsky. On the distribution of local current density along the PEM fuel cell cathode channel. *Electrochim. Comm.*, 101:35–38, 2019. doi:10.1016/j.elecom.2019.02.005.

³¹T. Suzuki, Y. Nakata, F. Tsutsui, and S. Tsushima. Investigation of gas transport properties of PEMFC catalyst layers using a microfluidic device. *J. Electrochem. Soc.*, 167:124519, 2020. doi: 10.1149/1945-7111/abaf28.

³²K. Shinozaki, H. Yamada, and Yu Morimoto. Relative humidity dependence of Pt utilization in polymer electrolyte fuel cell electrodes: Effects of electrode thickness, ionomer-to-carbon ratio, ionomer equivalent weight, and carbon support. *J. Electrochem. Soc.*, 158: B467–B475, 2011. doi:10.1149/1.3556906.

NOMENCLATURE

\sim	Marks dimensionless variables
A_λ	Dimensionless parameter, Eq.(13)
a_w	Water vapor activity
B_L	Dimensionless parameter, Eq.(13)
b	ORR Tafel slope, V
c	Oxygen molar concentration in the CCL, mol cm ⁻³
c_b	Oxygen molar concentration in the GDL, mol cm ⁻³
c_h	Oxygen molar concentration in the channel, mol cm ⁻³
c_{ref}	Reference oxygen molar concentration, mol cm ⁻³
c_w	Water molar concentration in the membrane, mol cm ⁻³
c_v^s	Saturated water concentration at 80°C
C_{dl}	Double layer volumetric capacitance, F cm ⁻³
D_b	Oxygen diffusivity of the GDL, cm ² s ⁻¹
D_w	Water diffusivity of the membrane, cm ² s ⁻¹
D_{ox}	Oxygen diffusivity of the CCL, cm ² s ⁻¹
$D_{ox,d}$	Oxygen diffusivity of the dry CCL, cm ² s ⁻¹
e_0	Elementary charge, C
F	Faraday constant, C mol ⁻¹
h	Cathode channel height, cm
i	Imaginary unit
i_*	ORR volumetric exchange current density, A cm ⁻³
j_0, j^0	Static current density, A cm ⁻²
K_L	CCL liquid water permeability, cm ²
k_{pe}	Slope of the water retention curve, Eq.(25), Pa
k_σ	Coefficient in Eq.(26) S cm ⁻¹
k_L	Liquid water transport coefficient, mol cm ⁻¹ Pa ⁻¹ s ⁻¹
L_{cab}	Cable inductance, H
l_b	GDL thickness, cm
l_m	Membrane thickness, cm
l_t	CCL thickness, cm
N_w	Water flux in the membrane, mol cm ⁻² s ⁻¹
n_d	Water drag coefficient in the membrane
p	Dimensionless parameter, Eq.(16)
p_c	Capillary pressure, Pa
p_g	Gas phase pressure, Pa
p_L	Liquid phase pressure, Pa
p_{O_2}	Oxygen partial pressure, Pa
p_{cell}	Cathode pressure, Pa
Q_{ORR}	ORR rate, A cm ⁻³
R	Gas constant, J K ⁻¹ mol ⁻¹
R_{HFR}	High frequency cell resistivity, Ohm cm ²
s	CCL liquid saturation
s_0	Minimal CCL liquid saturation, Eq.(25)
t_*	Characteristic time of DL charging, s
V_w	Liquid water molar volume, cm ³ mol ⁻¹
W_m	Ionomer equivalent weight, g mol ⁻¹
v	Air flow velocity in the channel, cm s ⁻¹
x	Coordinate through the cell, cm
z	Coordinate along the channel, cm
Z_{seg}	Segment impedance, Ohm cm ²
Z_{cell}	Cell impedance, Ohm cm ²

Subscripts:

0 membrane/CCL interface
 b GDL
 ref Reference value
 h Channel

Superscripts:

0 Steady-state value
 1 Small-amplitude perturbation

Greek:

α_s Dimensionless parameter in Eq.(4)
 α_w Net water transfer coefficient in membrane
 η ORR overpotential, positive by convention, V
 Λ Membrane water sorption isotherm
 λ Membrane water content
 λ_c Air flow stoichiometry
 μ_w Liquid water kinematic viscosity, Pa s
 ρ_m Mass density of a dry ionomer, g cm⁻³
 σ_p CCL proton conductivity, S cm⁻¹
 σ_* Reference proton conductivity, S cm⁻¹
 ω Angular frequency of the AC signal, s⁻¹